Molecule Crowding Strategy in Polymer Electrolytes Inducing Stable Interfaces for All-Solid-State Lithium Batteries

Hong Zhang, Jiahui Deng, Hantao Xu, Haoran Xu, Zixin Xiao, Fan Fei, Wei Peng, Lin Xu, Yu Cheng, Qin Liu, Guo-Hua Hu,* and Liqiang Mai**

All-solid-state lithium batteries with polymer electrolytes suffer from electrolyte decomposition and lithium dendrites because of the unstable electrode/electrolyte interfaces. Herein, a molecule crowding strategy is proposed to modulate the Li^+ coordinated structure, thus in situ constructing the stable interfaces. Since 15-crown-5 possesses superior compatibility with polymer and electrostatic repulsion for anion of lithium salt, the anions are forced to crowd into a Li^+ coordinated structure to weaken the Li^+ coordination with polymer and boost the Li^+ transport. The coordinated anions prior decompose to form LiF-rich, thin, and tough interfacial passivation layers for stabilizing the electrode/electrolyte interfaces. Thus, the symmetric Li–Li cell can stably operate over 4360 h, the $LiFePO_4$||Li full battery presents 97.18% capacity retention in 700 cycles at 2 C, and the NCM811||Li full battery possesses the capacity retention of 83.17% after 300 cycles. The assembled pouch cell shows excellent flexibility (stand for folding over 2000 times) and stability (89.42% capacity retention after 400 cycles). This work provides a promising strategy to regulate interfacial chemistry by modulating the ion environment to accommodate the interfacial issues and will inspire more effective approaches to general interface issues for polymer electrolytes.

1. Introduction

Lithium metal anode possessed the highest theoretical specific capacity (3860 mAh g^{-1}) and lowest potential (−3.040 V vs standard hydrogen electrode) has been regarded as a promising anode for next-generation lithium batteries.[1] When it combines with a Ni-rich layered oxide cathode, the assembled lithium metal batteries (LMBs) are considered as the satisfactory choice to achieve high energy density in electrochemical energy storage systems.[2] However, the safety issue of LMBs with liquid electrolytes should not be ignored.[3] Developing all-solid-state lithium metal batteries (ASSLMBs) with high safety, satisfactory performances, and superior energy density is a vital approach to get rid of potential safety hazards and break through the bottleneck of LMBs employed liquid electrolytes.[4] Thus, various all-solid-state electrolytes (ASSEs) have been applied to the construction of ASSLMBs.[5] Among these, polymeric materials bestowed favorable processability and safety are considered as a desired candidate for ASSEs.[6] Especially, the outstanding flexibility of solid-state polymer electrolytes (SPEs) can be appreciated for folding ASSLMBs, which is deemed to be a key component for emerging flexible and wearable electronic devices.[7]

However, two essential challenges for further practical development of SPEs are lithium-ion transport and interfacial stability.[8] Numerous efforts have been attempted on boosting the conductivity of SPEs, but the interfacial stability has not received enough attention.[9] In fact, the unstable interfaces between the SPEs and electrodes affect the electrochemical performance of the ASSLMBs due to the continuous side reactions during cycling.[10] At the anode side, the chemical and mechanical instabilities at the SPEs/lithium metal interface are the dominant reason for electrochemical performance deterioration. As the strong reducibility of lithium metal, the oxidation process of SPEs occurs by dehydrogenation for uneven lithium deposition.[11] Moreover, the shear modulus of SPEs hardly reach the critical value (1–10 GPa) to prevent the uncontrollable dendrite growth and stripping in repeated cycling, leading to the formation of dead lithium and the facilitation of side reactions at the

H. Zhang, J. Deng, H. Xu, H. Xu, Z. Xiao, F. Fei, W. Peng, L. Xu, Y. Cheng, Q. Liu, L. Mai
State Key Laboratory of Advanced Technology for Materials Synthesis and Processing
School of Materials Science and Engineering
Wuhan University of Technology
Wuhan 430070, China
E-mail: linxu@whut.edu.cn; mlq518@whut.edu.cn

L. Xu, L. Mai
Hubei Longzhong Laboratory
Wuhan University of Technology (Xiangyang Demonstration Zone)
Xiangyang, Hubei 441000, China

L. Xu, L. Mai
Hainan Institute
Wuhan University of Technology Sanya
Wuhan 572000, China

G.-H. Hu
Université de Lorraine
CNRS, LRGP, Nancy F-54001, France
E-mail: guo-hua.hu@univ-lorraine.fr

The ORCID identification number(s) for the author(s) of this article can be found under https://doi.org/10.1002/adma.202403848

DOI: 10.1002/adma.202403848

SPEs/lithium metal anode interface, and finally damages the battery performances.[12] Besides, most SPEs possess low ionic conductivity at room temperature, so they need to be operated at elevated temperatures, which further reduces their elastic stiffness and raises the risk of dendrite piercing through electrolytes.[13] At the cathode side, strong oxidation of transition metal ions (TMs) at the high charge state and the irreversible lattice oxygen loss will catalyze the SPEs undergo an oxidative decomposition.[14] In addition, during the charging process, the hydrogen atoms in the weakened C—H bonds of the polymer are easy to take away by the anions of lithium salt to form acids, aggravating the side reactions on the SPEs/cathode interface and consequently degrading the electrochemical performances.[15] Much worse, the TMs migrate from the cathode to deposit onto the lithium metal anode, namely notorious transition metal crosstalk, lead to the heterogeneous SEI growth and lithium deposition and acting as the catalyst for electrolytes degradation, resulting in significant batteries capacity fade.[16]

Significant advancements have been reported in recent decades to handle the above-mentioned challenges related to interfacial stability. The direct strategy involves electrodes modification, such as cathode surface coating strategy and interfacial protection layer building in lithium metal anode.[17] Unfortunately, this way leads to an inevitably partially loss of volume/mass-energy density. Another electrolyte system construction strategy including polymers components regulation, novel lithium salts design, and innovative additives introduction.[18] Yet, none of single polymer has a board enough intrinsic band gap to simultaneously achieve the dendrite-free deposition in lithium metal anode and lithium ions extraction from high-voltage cathode during the charging process without electrolyte oxidation decomposition.[19] Thus, the concepts of gradient SPEs and double (multi)-layer SPEs are proposed to meet the requirement of simultaneously stabilizing the cathode and anode.[20] Additionally, the homogeneous electrode/electrolytes interface in situ construction by electrochemical methods in ASSLBMs is also considered as an effective strategy with the advantage of superior electrode/electrolytes interface compatibility, simple preparation technics, and safety.[21] A typical example is the lithium salt anion-induced decomposition to form a dense inorganic-rich interfacial layer. Nevertheless, this approach requires a higher lithium salt concentration to sustain the anion sacrifice, thus the polymer will confront the harsh demands of low glass-transition temperature (T_g), superior lithium salt solubility, and desirable mechanical performance. Therefore, precise regulation of interfacial chemistry and prevention of excessive decomposition of electrolytes are urgently demanded.

Herein, polyethylene oxide, the most widely employed SPEs in current, is chosen as a representative to solve the unstable electrode/electrolytes interface in ASSLBMs. As the reactive terminal —OH group in polyethylene oxide can react with lithium metal anode and be first oxidized at the voltage over 4.05 V leading the poor interfacial stability,[22] we proposed a molecule crowding strategy to modulate the Li^+ coordinated structure and consequently in situ regulate interfacial chemistry for stabilizing the electrode/electrolyte interface of ASSLMBs. Based on the similar molecular structure with polyethylene oxide chains and the weak supramolecular interaction with lithium ions, 15-crown-5 is introduced to SPE for destroying the crystallization of the polymer matrix and facilitating the dissociation of lithium salts. Since 15-crown-5 possesses superior compatibility with polyethylene oxide and electrostatic repulsion for $TFSI^-$ anion, the abundant anions are limited by forcing into the Li^+ coordinated sheath and then weaken the Li^+ coordination with $—CH_2CH_2O—$ (EO) group in polyethylene oxide, thus boosting the Li^+ transport. The reduction of confined anions is boosted and the anions prone to decompose at the electrolyte–anode interface to form LiF-rich SEI with fast Li^+ diffusion rate to achieve uniform lithium deposition. The inorganic compound contents in SEI boost the Young's modulus for preventing the lithium dendrites' growth and penetration of the interface. Also, the thin and tough CEI presented LiF-rich inner is beneficial to preventing continuous polymer degradation and transition-metal crosstalk (**Figure 1a**). As a result, the symmetrical Li–Li cells employed polyethylene oxide electrolytes with 15-crown-5 added ($PEOC_{15}$) could ultrastably operate about half a year, and the assembled all-solid-state $LiFePO_4||PEOC_{15}||Li$ full batteries display high-rate and long-cycle life. The $LiNi_{0.8}Co_{0.1}Mn_{0.1}O_2||PEOC_{15}||Li$ full batteries also present satisfactory capacity retention cycling at high voltage. Particularly, the pouch cells display superior flexibility and stability by employing this easily obtained and large-scale preparation of this SPE.

2. Results and Discussion

2.1. Investigation of Li^+ Coordinated Structure Modulating by 15-Crown-5

As Figure S1 (Supporting Information) shows, the rigid cyclic 15-crown-5 possesses a similar molecule structure with polyethylene oxide, leading to superior compatibility in polymer matrix. And the C—O—C groups in 15 crown-5 show nucleophilicity and electronegativity, which promotes lithium salt dissociation and presents electrostatic repulsion for anion (Figure S2, Supporting Information).[23] Further, the density functional theory calculation was applied to explore the binding energy between Li^+ and other groups in $PEOC_{15}$. The binding energy of 15-crown-5-Li^+ (−4.714 eV) is higher than that of EO groups (−2.865 eV), and lower compared to $TFSI^-$ (−5.015 eV), which also indicates the introduction of 15-crown-5 presents the potential for assisting the dissociation of LiTFSI, thus promoting the quantity of Li^+ in $PEOC_{15}$ electrolyte (Figure S3, Supporting Information). The molecular dynamics (MD) simulations were employed to reveal the influence of 15-crown-5 on the Li^+ coordinated structure. The results of the 3D snapshot, obtained radical distribution functions (RDF), and corresponding running Li^+ coordination numbers (CN) are shown in Figure 1b–e. In the PEO electrolyte, the Li^+ strongly coordinates with EO chains and the Li^+ shows the multi-coordinated structure with EO groups. It is widely known that polyethylene oxide with a high oxygen atomic ratio presents readily Li^+ coordinated ability to form stable single-chain helical configurations around the lithium ions. The Li^+ is transported by hopping and shuttling between solvation sites consisted of Lewis-basic oxygens of EO chains, and promoted by polymer segment chains motion. Nevertheless, this stable binding construction significantly restricts the movement of lithium ions with electrochemical-active.[24] The CN of the first coordinated sheath is 5.12. Only a fraction of $TFSI^-$ observed in the first coordinated

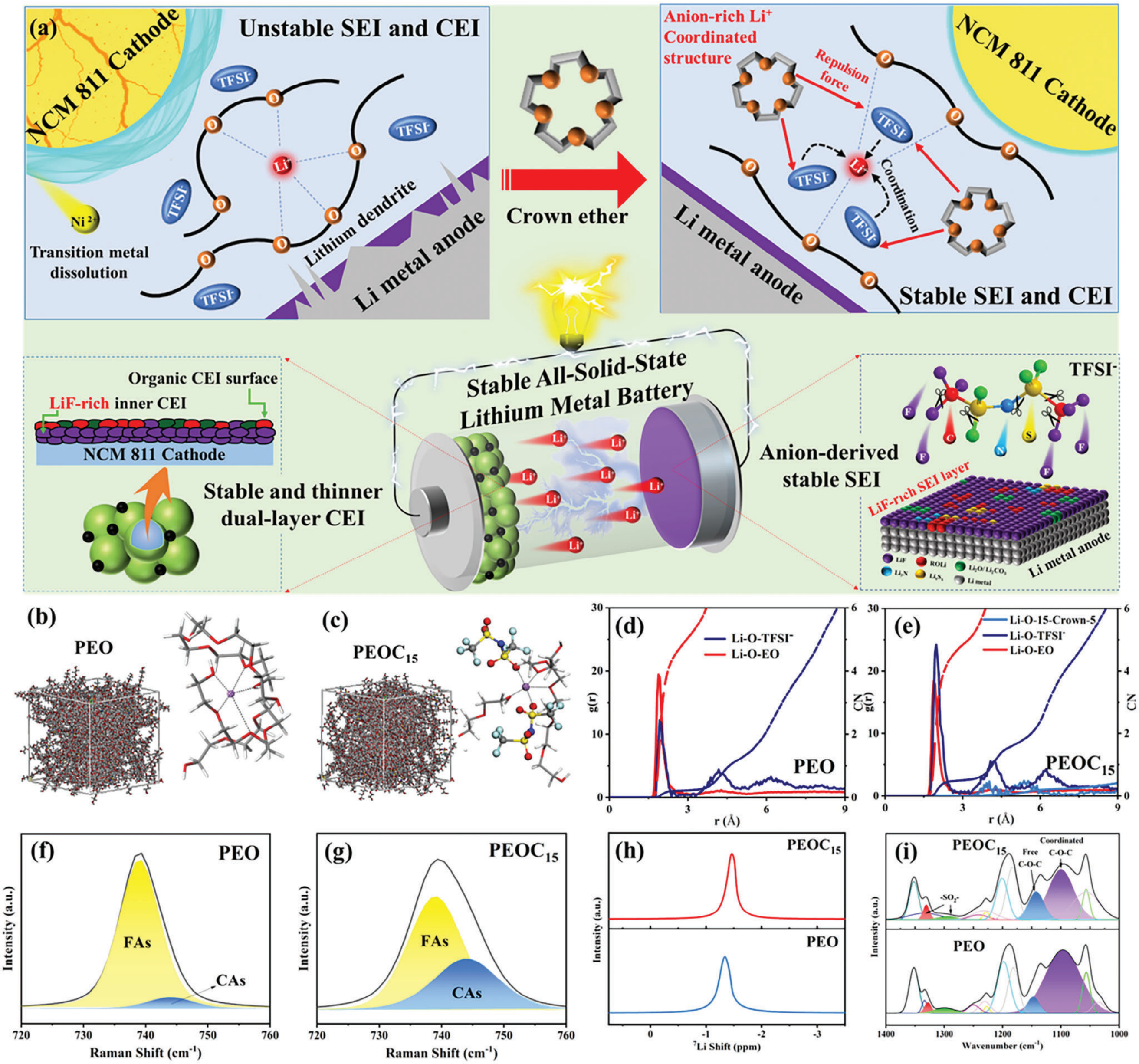

Figure 1. Schematic diagrams and characterization of Li^+ coordinated structure modulation. a) schematic diagrams of molecule crowding strategy based on 15-crown-5 inducing the anion-rich Li^+ coordinated structure for stable electrode/electrolytes interfaces in ASSLBMs. 3D snapshot of b) PEO electrolyte and c) $PEOC_{15}$ electrolyte system obtained from MD simulations and partially enlarged snapshot representing Li^+ coordinated structure. RDF g(r) and CN of the Li-O-PEO, Li-O-$TFSI^-$, and Li-O-15-crown-5 pairs calculated from MD simulation trajectories in d) PEO electrolyte and e) $PEOC_{15}$ electrolyte. Raman spectra of f) PEO and g) $PEOC_{15}$ electrolytes. h) ^7Li solid-state NMR spectra and i) FTIR spectra of PEO and $PEOC_{15}$ electrolytes.

sheath of Li^+ (CN = 0.235) through Li^+-O_{TFSI} coordination. Instead, the $PEOC_{15}$ electrolyte presents the obvious changes of enhanced CN_{TFSI^-} (0.507) and decreased CN_{EO} (CN = 4.89). Especially, the 15-crown-5 is hardly observed in the first coordinated sheath of Li^+. The decreased CN_{EO} indicates this stable Li—O binding construction becomes weakened, resulting in significantly promoting Li^+ movement.[25] Besides, the enhanced CN_{TFSI^-} means that more anions are confined in the Li^+ coordinated sheath attributed to the molecule crowding effect caused by employing the 15-crown-5. As a result, the abundant anions are forced into the Li^+ coordinated sheath to form an anion-rich coordinated structure.[26] The differences of the coordinated sheath of Li^+ between $PEOC_{15}$ and PEO electrolyte is due to the ability of Li^+ coordinated with other atoms or groups is finite, specifically, the more $TFSI^-$ anions coordinate with Li^+ will inevitably decrease the Li–O coordination between Li^+ and polyethylene oxide. Raman spectra were employed to investigate the coordination capabilities by comparing the S—N—S stretching peaks of $TFSI^-$ anions in the electrolytes and can be divided into two peaks assigning of free anions (FAs) and coordinated anions (CAs), respectively.[27] The integral intensity decrease of the FAs peak proves that more TFSI$^-$ anions are confined in the coordinated sheath when 15-crown-5 introducing (Figure 1f,g).[28] The ^{7}Li solid-state nuclear magnetic resonance (NMR) spectra was performed to indicate the changes of the Li$^+$ chemical environment. Compared with the PEO electrolyte, the peak in the ^{7}Li solid-state NMR spectrum of PEOC$_{15}$ electrolyte shifts 0.12 ppm upfield, implying the higher electron density around Li$^+$, which corresponds with the incline of CN$_{\mathrm{TFSI}^-}$ obtained from the MD simulations (Figure 1h).[29] Fourier transform infrared spectrometer (FT-IR) was employed to observe the evidence of Li$^+$ coordinated structure modulation. The characteristic peaks of asymmetric —SO$_2$— in PEO electrolyte are observed at 1328 and 1299 cm^{-1}, while the peaks shift to 1331 and 1294 cm^{-1} in PEOC$_{15}$ electrolyte, indicating the enhanced interaction between lithium ions and oxygen atoms in the sulfonic acid groups of TFSI$^-$ anions.[30] The characteristic peaks of C—O—C vibration can be divided into the coordinated C—O—C vibration at ≈1100 cm^{-1} and the free C—O—C vibration at ≈1150 cm^{-1}.[31] When 15-crown-5 inducing, the coordinated C—O—C vibration is significantly reduced, indicating the weakened coordinating capability of EO groups surrounding Li$^+$ and more TFSI$^-$ anions into the coordinated sheath (Figure 1i; Figure S4, Supporting Information).

2.2. Characterization and Electrochemical Performance of PEOC$_{15}$ Electrolyte

The large-scale prepared PEOC$_{15}$ electrolyte membrane presents a transparent appearance (Figure S5, Supporting Information), and possesses a smooth surface (the fluctuation of surface height is less than 2 nm), resulting in pretty contact with electrodes (Figure S6, Supporting Information). The mechanical properties of the PEOC$_{15}$ electrolyte membrane were investigated by stress–strain (σ–ϵ) curves shown in **Figure** 2a. The tensile modulus, tensile strength, and elongation at break of PEOC$_{15}$ electrolyte membrane were tested as 281.05, 86.81 MPa and 85.49%, while those of PEO electrolyte membrane are 198.67, 72.07 MPa and 149.85%, respectively, which proves the rigid ring structure of 15-crown-5 and the hydrogen bond between 15-crwon-5 and terminal —OH of polyethylene oxide endow the PEOC$_{15}$ electrolyte membrane with higher rigidity. The thermostability of PEOC$_{15}$ and PEO electrolyte membrane was characterized by thermogravimetric analysis (TGA). Apparently, the PEOC$_{15}$ electrolyte membrane presents superior thermostability compared with the PEO electrolyte membrane because of the higher thermogravimetric temperature and char yield reflected from Figure 2b. Differential scanning calorimetry (DSC) was employed to characterize the glass transition temperature (T_g) and the degree of crystallization. The PEO electrolyte presents a T_g of −39.26 °C, while the T_g of the PEOC$_{15}$ electrolyte is evidently decreased to −44.39 °C, illustrating the boosted free mobility of the polymer chain. The 15-crown-5 presents high compatibility with polymer, which weakens the intermolecular interaction between polymer chains and destroys the neat arrangement of polymer chains, thus leading the decrease of T_g. The dramatically reduced crystal enthalpy (decreased ≈85%) of PEOC$_{15}$ electrolyte indicate the crystallization degree is declined, proving the 15-crown-5 possesses external plasticization for destroying the crystalline region of polyethylene oxide, thus broadening the Li$^+$ transport paths (Figure 2c). This result matches the characteristics weakened peak intensity in the XRD pattern of the PEOC$_{15}$ electrolyte (Figure 2d). In addition, the enhanced melting temperature (T_m) of PEOC$_{15}$ electrolyte is found due to the formation of hydrogen bond between the terminal —OH of polyethylene oxide and the C—O—C group of 15-crown-5, contributing to the continuous operation of PEOC$_{15}$ electrolyte at higher temperature.

Several electrochemical measurement technologies were employed to investigate the potential of PEOC$_{15}$ electrolyte on applying in the LBMs. The 5 wt.% 15-crown-5 added PEOC$_{15}$ presents the superior intrinsic ionic conductivity of 1.22 × 10^{-4} S cm^{-1} at room temperature and 6.17 × 10^{-4} S cm^{-1} at 60 °C, compared with 6.67 × 10^{-6} S cm^{-1} and 1.08 × 10^{-4} S cm^{-1}of PEO electrolyte, respectively (Figure 2e; Figure S8, Supporting Information). The lower activation energy (E_a, 63.00 kJ mol^{-1} of PEO electrolyte and 32.19 kJ mol^{-1} of PEOC$_{15}$ electrolyte) calculated according to the Arrhenius diagram proves the lower energy barrier for lithium-ion transport, thus leading to the rapid lithium ion transport in PEOC$_{15}$ electrolytes (Figure 2f). The Li$^+$ transference number of the PEOC$_{15}$ electrolyte is calculated to be 0.53, which outclasses the PEO electrolyte of 0.17. (Figure 2g; Figure S9, Supporting Information). This result is attributed to the higher Li$^+$ concentration and confined FAs movement. The electrochemical window of SPEs measured by linear sweep voltammetry (LSV). The PEOC$_{15}$ electrolyte also gains a higher electrochemical window of 5.2 V, while the PEO electrolyte is gradually oxidized as the voltage over 4 V (Figure 2h). The interfacial stability during the lithium-ion stripping and plating process was investigated by galvanostatic cycling test using the assembled symmetrical lithium cells. We first observe the critical current density (CCD) of electrolytes, and the CCD of PEOC$_{15}$ and PEO electrolytes shown in Figure S10 (Supporting Information) are 0.3 and 0.7 mA cm^{-2}, respectively. Apparently, PEOC$_{15}$ electrolytes can withstand higher current density because of the higher lithium-ion conductivity.[32] Then, the cycling performances of PEOC$_{15}$ and PEO electrolytes are comparatively investigated in Figure 2i. The polarization voltage of the cell with PEO electrolyte is rapidly and continuously increased, and finally breaks down after 200 h, which is due to the inferior interface contact and stability between PEO electrolyte and lithium metal. When introducing the 15-crown-5, the polarization voltage obviously declines and the cycling time vastly boosts. Astonishingly, the PEOC$_{15}$ electrolyte displays a relatively steady cycling and the longest cycling life of 4360 h (about half a year), and the enhancement of polarization voltage is hardly observed (Figure S11, Supporting Information), which exhibits the advancement compared with previously reported all-solid-state polymer-based electrolytes presented in Figure S12 and Table S3 (Supporting Information). The lithium deposition behavior is also investigated. As the outstanding lithium deposition performance with PEOC$_{15}$ in symmetrical lithium cells, the assembled Li–Cu asymmetrical cells were applied to further evaluate the true utilization of lithium metal and stability of SEI formed at the interface without being aided by extra lithium ions from the other lithium symmetric electrode. The coulombic efficiency (CE) of PEOC$_{15}$ and PEO electrolytes is presented in Figure 2j. The CE of the PEOC$_{15}$ electrolyte is stable at 96% and continues over 300 cycles without showing CE instability. For comparison, the CE of PEO electrolyte only

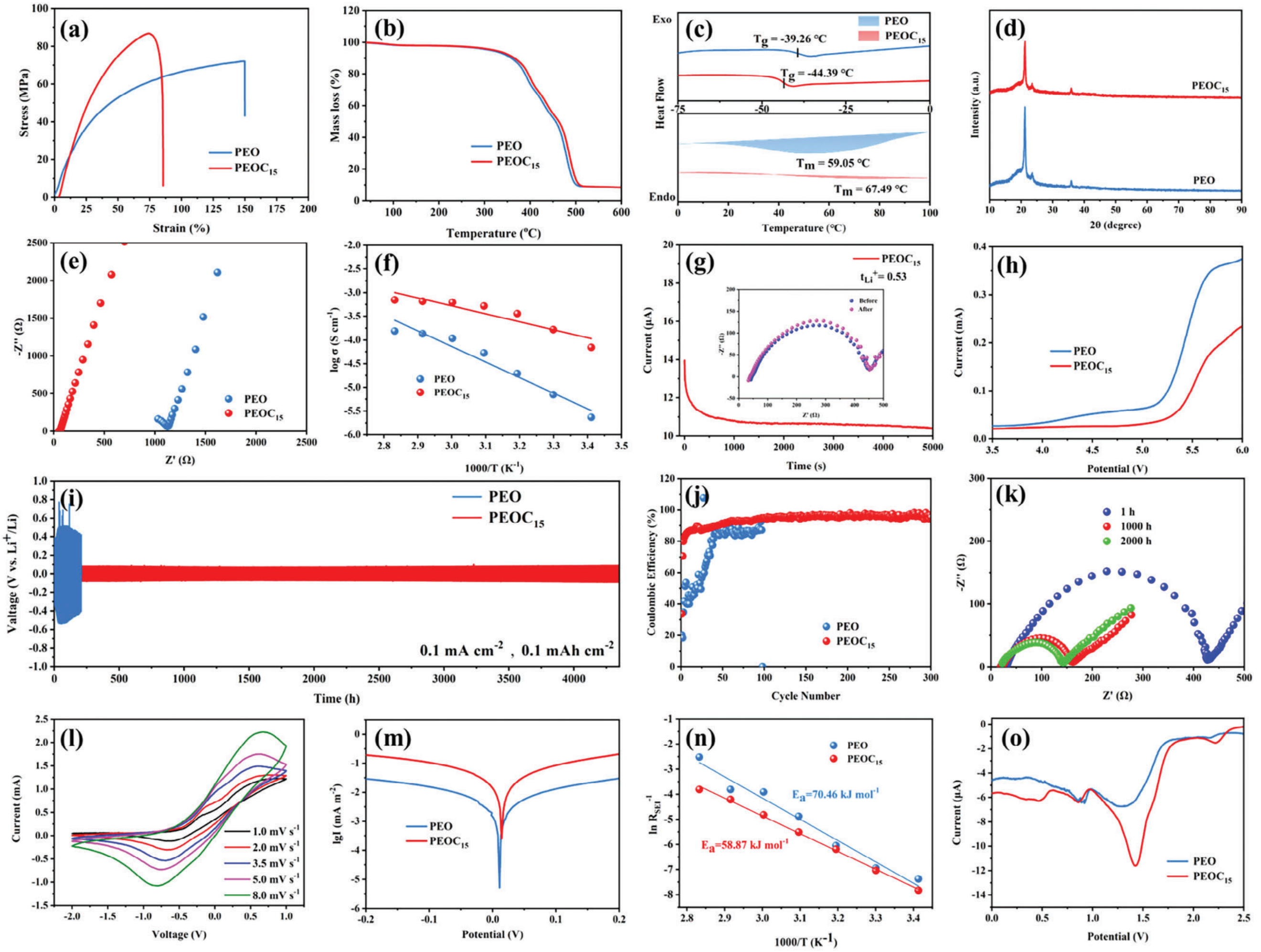

Figure 2. The physical and chemical characterization, lithium-ion transport properties, and lithium deposition performance by adding 15-crown-5 in SPEs. a) σ–ϵ curves, b) TGA curves, c) DSC curves, and d) XRD patterns of PEO and PEOC$_{15}$ electrolytes. e) EIS curves of PEO and PEOC$_{15}$ electrolytes at room temperature. f) Arrhenius plots of PEO and PEOC$_{15}$ electrolytes at different temperatures. g) Current–time curve following DC polarization of Li||PEOC$_{15}$||Li symmetrical cell at 10 mV s^{-1} (inset: EIS variation before and after polarization at 60 °C). h) LSV curves of PEO and PEOC$_{15}$ electrolytes. i) Galvanostatic cycling of symmetric lithium cells with PEO and PEOC$_{15}$ electrolytes at 60 °C. j) Coulombic efficiencies of Li plating/stripping in Li–Cu cells using PEO and PEOC$_{15}$ at 0.2 mA cm^{-2}, 0.2 mAh cm^{-2} and 60 °C. k) Alternating current impedance profiles of Li||PEOC$_{15}$||Li at different cycles. l) CV curves of Li||PEOC$_{15}$||Li cell at different voltage scan rates from 1.0 to 8.0 mV s^{-1} m) Tafel curves of the Li||PEO and Li||PEOC$_{15}$ interfaces from the linear sweep voltammetry tests. n) Linearly fitted graph of the relationship between ln ($R_{\mathrm{SEI}}{}^{-1}$) and T^{-1}. o) CV curves of reduction behavior of PEO and PEOC$_{15}$ electrolytes.

reaches the highest 88.89% after several cycles, and the Li–Cu cell breaks down less than 100 cycles. Besides, we can clearly observe that the uniform lithium deposition by using PEOC$_{15}$ electrolyte while that of PEO is uneven, which demonstrates the introduction of 15-crown-5 contributed to uniform lithium deposition (Figure S13, Supporting Information).

2.3. Investigation on Electrode/Electrolyte Interface Chemistry Regulated by 15-Crown-5

The electrochemical properties of solid electrolyte interface (SEI) are first characterized. Figure 2k reflects the impedance spectrum of the Li||PEOC$_{15}$||Li cell after different cycling times. The impedance spectrum curves can be divided into the R_s (resistance in bulk electrolytes) and the R_{SEI} (reaction resistance at electrode/electrolyte interface). The R_s and R_{SEI} of lithium symmetrical cell decreases gradually as the cycling times increase, proving the interface contact and compatibility of lithium metal enhances, which illustrates the PEOC$_{15}$ electrolyte possesses a self-adapting effect.[33] The diffusion coefficients of Li$^+$ across the SEI quantitative calculated by Randles–Sevick equation according to the cyclic voltammetry (CV) testing for SEI formed on Li||PEOC$_{15}$||Li cell is 3.15 × 10^{-13} m^2 S^{-1}, which is higher than that of Li||PEO||Li cell (Figure 2l; Figure S14, Supporting Information).[34] Tafel curves were also obtained by the results of CV measurements (Figure 2m; Figure S15, Supporting Information). The lithium anode with PEOC$_{15}$ electrolyte presents an obvious enhancement of exchange current density of 0.039 mA cm^{-2} instead of 0.007 mA cm^{-2} for the lithium anode with PEO electrolyte, indicating faster interface ionic transfer kinetics of the SEI formed by employing $PEOC_{15}$ electrolyte.[35] The lithium-ion diffusion energy barrier (E_a) through the SEI was calculated by the EIS results of the Li||PEO||Li and Li||$PEOC_{15}$||Li symmetric cells tested at different temperatures (from 293 to 353 K) and the Nyquist points were fitted by the equivalent circuit model (Figure S16, Supporting Information). As the linear fitting results between ln ($R_{SEI}{}^{-1}$) and T^{-1} shown in Figure 2n, the calculated E_a for the lithium anode with $PEOC_{15}$ electrolyte (58.87 kJ mol^{-1}) is much lower than that of the lithium anode with PEO electrolyte (70.46 kJ mol^{-1}), indicating the enhanced Li^+ diffusion rate through the SEI on the lithium anode.

The formation and composition of the SEI are subsequently investigated. Generally, the polymer and anions can be reduced to a variety of organic/inorganic species to form SEI depend on the potential. Apparently, a stronger decomposition peak attributed to the $TFSI^-$ anion is found at 1.41 V in the curve of $PEOC_{15}$ electrolyte, while that of PEO electrolyte appears in 1.36 V, meaning the employment of 15-crown-5 promotes the reduction of $TFSI^-$ anions, which will generate the inorganic components in SEI. Moreover, the higher reduction potential of $TFSI^-$ anion in $PEOC_{15}$ electrolyte illustrates the earlier decomposition of $TFSI^-$ anion, which is attributed to the more $TFSI^-$ anion coordinated with the Li^+ in $PEOC_{15}$ electrolyte (Figure 2o). In addition, compared with the degradation peak of the polymer at 0.92 V in the PEO electrolyte, the lower peak at 0.86 V in the $PEOC_{15}$ electrolyte illustrates the reductive stability of polymer also boosts due to the 15-crown-5 added.[36] The X-ray photoelectron spectroscopy (XPS) was performed to investigate the composition of the SEI on the surface of the lithium metal anode after cycling with the PEO and $PEOC_{15}$ electrolytes (Abbreviated as SEI_{PEO} and SEI_{PEOC15}), and the **Figures** 3a–d and S17 (Supporting Information) give the high-resolution spectra of C 1s, O 1s, F 1s, N 1s, and S 2p. For the SEI_{PEO}, the C 1s spectrum can be divided into five peaks at a binding energy of 284.8, 286.8, 288.2, 289.6, and 293.1 eV assigning to C—C, C—O, C═O, $ROCO_2Li$ and -CF_3 respectively. As for SEI_{PEOC15}, the peak of Li_2CO_3 is discovered (290.0 eV), while the $ROCO_2Li$ and —CF_3 peak is hardly seen. The C—C, C—O, C═O, $ROCO_2Li$ and Li_2CO_3 signals can be attributed to the oxidative decomposition of polyethylene oxide in the electrolyte, while the —CF_3 signal comes from $TFSI^-$. The O 1s signals of SEI_{PEO} are curve-fitted into two peaks with binding energies of 531.0 and 532.8 eV, separately representing C═O and C—O. Besides, the two new peaks represented Li_2CO_3 (531.8 eV) and Li_2O (528.4 ev) are found in the O 1s spectrum of the SEI_{PEOC15} area. We consequently investigate the areal ratio of C—C and C—O peaks. The C—C/C—O ratio of SEI_{PEO} and SEI_{PEOC15} are 2.183 and 5.267, respectively. Apparently, the content of the C—O signal in the SEI surface reduces when 15-crown-5 is employed. The differences reflect by C 1s and O 1s spectra indicate the degradation of polyethylene oxide is inhibited.[37] And the appearance of Li_2CO_3 and Li_2O also proves the degradation pathway of the polymer is changed. The F 1s, N 1s, and S 2p of SEI_{PEOC15} prove the existence of Li_3N, LiF, and Li_2S (Li_2S_2). As the N, F, and S elements only originated from $TFSI^-$ and the LiTFSI possesses the lowest LUMO (lower unoccupied molecular orbital) level (Figure S18, Supporting Information), there are reasons to believe that the decomposition of $TFSI^-$ at the anode interface generates the above-mentioned inorganic components in SEI.[38] The suppressed polymer degradation and prior decomposition of $TFSI^-$ are attributed to an anion-rich Li^+ coordinated structure induced by 15-crown-5. The participation of $TFSI^-$ in Li^+ coordinated structure not only boosts the reductive stability of the polymer but also enhances the reduction of themselves. Specifically, coordinated $TFSI^-$ is prone to accept the electron and get reduced, leading the formation of inorganic species.[39]

We further investigated the SEI main components distribution by the time-of-flight secondary ion mass spectroscopy (TOF-SIMS). The mass spectrum is partially presented in Figure S19 (Supporting Information). The C^-, O^-, Li^-, F^- and OH^- are apparently found, and the variety hydrocarbon compounds and lithium compound fragments are identified in negative mode. Among them, the C_2HO^- (representing organic species), $LiF_2{}^-$ (representing LiF), $CO_3{}^{2-}$ (representing Li_2CO_3 species), LiO^- (representing Li_2O species), LiS^- (representing Li_2S and Li_2S_2 species), and LiN^- (representing Li_3N) species were investigated.[40] The chemical mapping images of SEI main components are displayed in Figure S20 (Supporting Information). The highest $LiF_2{}^-$ signal intensity proves the LiF-rich interface between electrolytes and lithium anode. The depth profiles reflect the variation of signal intensity with the sputtering time, proving the outer layer and inner layer components of SEI are different, and the 3D rendering models of the top–down-depth sputtering further visually demonstrate the SEI compounds spatial distribution (Figure 3e). Apparently, the LiF is dominating distributed in the SEI layer. The Li_2S/Li_2S_2, Li_3N, Li_2O, and moderate organic oligomer mainly concentrate on the inner SEI, while Li_2CO_3 uniformly appears in the outer SEI layer. The inorganic lithium compounds, notably LiF, Li_3N, Li_2O, and so on, possess weak bonding with a high interfacial energy with lithium anode. They increase the lithium lateral diffusion along the SEI/Li interface and inhibit lithium metal from penetrating into the inorganic SEI layer. Especially, the co-existence of LiF and Li_2CO_3 promotes space charge accumulation along their interfaces, which not only generates a higher ionic carrier concentration and significantly improves lithium-ion transport and reduces electron leakage, but also further boosts the passivation function to suppress electrolyte decomposition.[41] Meanwhile, the incline of inorganic compound contents in SEI boosts the mechanical strength for better suppression of lithium dendrites growth and penetration of the interface. Instead, the organic SEI has a strong bonding with lithium ions, thus restricting the lithium diffusion along the SEI/Li interface and promoting vertical lithium penetration into the SEI to form lithium dendrites.[42] The mechanical property of the SEI is also crucial to affect the lithium electrodeposition uniformity since the lithium metal anode will experience a repeated interface displacement during electrochemical stripping and plating. When lithium deposition occurs at the interface, the local stress will be generated due to the deformation of the SEI, with a magnitude depending on Young's modulus. And the high stress concentration will enhance the risk of crack formation or even breakage.[43] As shown in Figure 3f, the average Young's modulus of SEI_{PEO} obtained by atomic force microscope (AFM) is 1.085 GPa. In comparison, that of SEI_{PEOC15} is 37 times greater than SEI_{PEO} (40.078 GPa, Figure 3g). The super high Young's modulus of SEI_{PEOC15} ensures the uniformly lithium metal

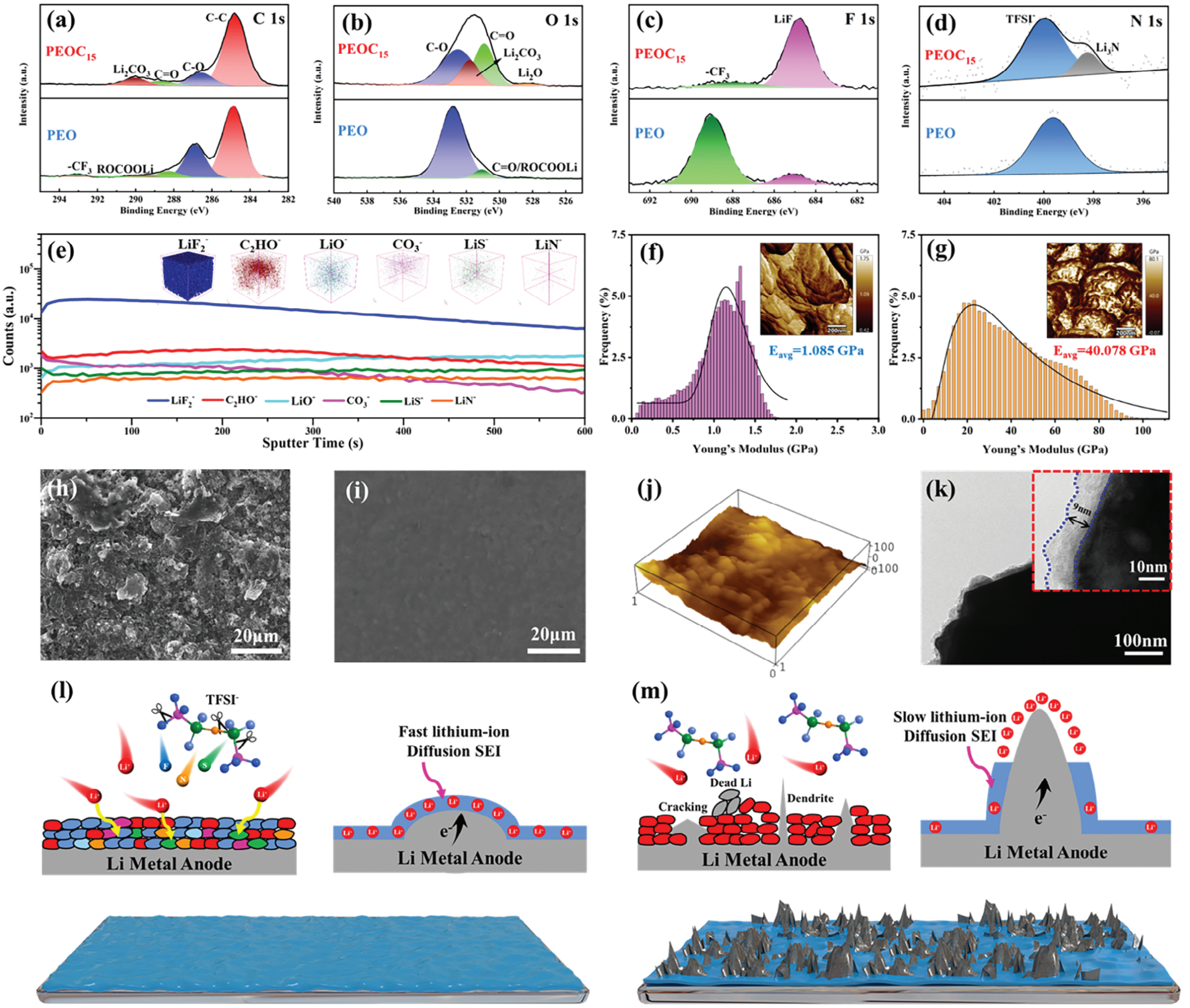

Figure 3. The characterization of LiF-rich SEI layer for withstanding the lithium dendrites. High-resolution XPS spectra of Li foils after cycling with the PEO and PEOC$_{15}$: a) C 1s, b) O 1s, c) F 1s, and d) N 1s. e) Depth profiles and 3D rendering models (inset) of the after cycling with PEOC$_{15}$ electrolyte. Histograms of Young's modulus of Li anode surface after cycling with f) PEO and g) PEOC$_{15}$ electrolyte (Inset: Young's modulus maps). Top view SEM images of Li anode surface in h) Li||PEO||Li and i) Li||PEOC$_{15}$||Li after cycling. j) AFM 3D images of Li anode surface in Li||PEOC$_{15}$||Li after cycling. k) TEM images of the SEI between the PEOC$_{15}$ electrolyte and lithium anode. Schematic diagram of lithium deposition mechanism by employing l) PEOC$_{15}$ and m) PEO electrolytes.

electrodeposition and dramatical reduction of stress concentration, thus improving the stability of the interface.

In order to explain the phenomena of stable cycling performances and uniform lithium deposition, we also investigated the surface morphology of lithium foil after cycling. The short-circuit cell with PEO electrolyte was taken apart, and the irregular surface with uneven particles is found in Figure 3h, proving the failure of the cell may be caused by lithium dendrites. Inversely, the surface of the lithium anode cycling over 4360 h with PEOC$_{15}$ electrolyte is still flat (Figure 3i). The AFM images displayed in Figure 3j and Figure S21 (Supporting Information) further reveal the uniform lithium deposition with hemispheric morphology and the fluctuation of surface height is less than 30 nm. Obviously, hemispheric lithium deposition presents a smooth surface without any sharp tip, thus preventing the serious safety hazards caused by lithium dendrite deposition. Moreover, hemispheric lithium deposition possesses minimum specific surface area, resulting in less SEI formed by the reactions between lithium metal and electrolyte, which leads to the superior CE and cycle life of batteries. The thickness of the homogeneous SEI layer between PEOC$_{15}$ electrolyte and lithium anode is measured to 9 nm according to the transmission electron microscope (TEM) images, and the elemental mappings obtained by energy disperse spectroscopy verify the uniform coexistence of C, O, S, and F (Figure 3k; Figure S22, Supporting Information).

In general, the lithium deposition process takes place under the SEI, including lithium ions migrating through SEI and following reduction to lithium atom by obtaining an electron. According to the above-mentioned analysis of the SEI component, the hemispheric lithium deposition mechanism is due to the fast lithium-ion diffusion SEI between the PEOC$_{15}$ electrolyte and lithium anode. During the lithium plating process, the initial lithium nucleation sites evolve into bumps distributed on the anode. When the SEI possesses a fast lithium-ion diffusion rate, the lithium ions migrate onto the anode surface with faster kinetics. As a result, the rate-determining step of lithium deposition is reaction-controlled and the number of lithium ions beneath the SEI remarkably increases even on the edges of lithium nucleation bumps. The conversion of lithium-ion to lithium atom occurs uniformly on lithium nucleation bumps, leading to hemispheric lithium deposition (Figure 3l). On the contrary, as the lithium-ion diffusion rate declines, it will become a diffusion-controlled reaction. The lithium-ion is difficult to get through the SEI so that the ions are easy to deplete, which results in lacking of lithium ions beneath SEI. The Li nucleation bump edges are unable to capture lithium ions under the electric field, and insufficient lithium ions preferentially tend to gather on the tip inducing the lithium dendrite formation (Figure 3m).[44]

As the polyethylene oxide-based SPEs will continuously oxidize at a voltage greater than 4 V, we also focus on enhancing cathode/electrolyte interfacial stability to broaden the electrochemical stability window by introducing 15-crown-5. The NCM811||Li batteries were assembled to investigate the performances of the cathode/electrolyte interface. **Figure 4a** indicates the current of the NCM811||Li battery with PEO electrolytes fluctuates when charging at a constant voltage of 4.6 V, while the maximum can withstand the oxidation voltage of the NCM811||Li battery increases to 4.8 V after introducing the 15-crown-5. The result of activation energy calculated according to Arrhenius' law proves the interfacial ion transfer energy barrier of the PEOC$_{15}$/NCM811 interface is lower than that of the PEO/NCM811 interface (Figure 4b). The EIS curves of NCM811||PEO||Li and NCM811||PEOC$_{15}$||Li batteries show the charge transfer resistance (R_{ct}) and the interface resistance (R_{if}) represented in the middle-frequency region. The resistance (R_{ct} + R_{if}) of NCM811||PEOC$_{15}$||Li battery is much lower than that of NCM811||PEO||Li batteries, indicating a better interfacial compatibility between PEOC$_{15}$ and cathode (Figure 4c).[20] Whereas, the resistance of NCM811||PEO||Li battery increases after 100 cycles due to the interfacial deterioration, while that of NCM811||PEOC$_{15}$||Li battery presents a surprising decline attributed to the stable interface construction between the electrode and electrolyte (Figure 4d). As shown in the SEM images, the cathode particle is visibly broken in the battery with PEO electrolyte after cycling, which causes the continuous electrolyte decomposition to enhance resistance (Figure 4e).[45] For comparison, the crack is hardly observed in the cathode of the NCM811||PEOC$_{15}$||Li battery, indicating the 15-crown-5 employment is beneficial for improving the electrochemical stability (Figure 4f).

As one of the important parts to affect the cathode/SPE interface, the morphology, structure, and components of CEI were investigated. As the high-resolution TEM image showed in Figure 4g, a thick and uneven amorphous layer is coated on the surface of PEO-based cycled NCM811 (NCM-PEO) particles. Instead, the CEI layer of NCM-PEOC$_{15}$ particles is thin and uniform, leading to lower interfacial resistance at the cathode/SPEs interface (Figure 4h). The XPS measurement was carried out to compare the components of CEI on the cycled NCM811 cathode surface. The strong C—O and C═O peaks in C 1s and O 1s spectra of NCM- PEOC$_{15}$ and NCM-PEO particles indicate the organic species on the CEI layer surface of NCM- PEOC$_{15}$ particles due to the inevitable PEO decomposition under the high voltage. In addition, the metal-C peak (represent the metal carbide) presented in the C 1s spectrum of NCM-PEO particles proves the transition metal dissolution, and the exited TM-O signal (represent the lattice oxygen in NCM811) in O 1s spectrum illustrates the nonuniform-CEI-layer of NCM-PEO particles. (Figure 4i,j).[46] Furthermore, the F 1s spectra and N 1s spectra show the contents of LiF, LiN$_x$O$_y$, and Li$_3$N on the CEI layer surface of NCM-PEOC$_{15}$ particles (Figure 4k,l). As an excellent insulator of electrons, LiF is expected to maximize its potential shielding function when it is located inside the CEI, while LiN$_x$O$_y$ and Li$_3$N distributed on the outside can effectively play the role as excellent Li$^+$ conductors. As compared, these profitable components are hardly observed for stable CEI on the surface of NCM-PEO particles. To gain more insights into inner CEI composition, a depth profile was further conducted using an in-depth Ar$^+$ sputtering for 0, 30, 60, 90, 120, and 150 s. Apparently, the weaker C—O and C═O signals illustrate the lower organic species in the inner CEI of NCM-PEOC$_{15}$ particles. Besides, a favorable CEI component of polycarbonate (Poly(CO$_3$)) is found at 291.0 eV in the C 1s spectrum and 534.5 eV in the O 1s spectrum in inner CEI, which is beneficial for mitigating the polarization at high voltage to avoid the possible local overcharge and severe polarization of the interface.[47] The stronger LiF signal show an inorganic prominent inner CEI composition. Inorganic-rich CEI can protect the cathode continuously since it suffers from less strain during cathode volume change. Furthermore, the signal of lattice oxygen in NCM811 appears early along with the etching process, demonstrating the generation of a thinner CEI on NCM-PEOC$_{15}$ particles (Figure 4m). The component of inner CEI on the surface of NCM-PEO particles is also analyzed according to the depth profile presented in Figure S24 (Supporting Information). Instead, the existed strength peaks of C—O, C═O, and ROCOOLi in C 1s and O 1s spectra prove the abundant organic component in the CEI of NCM-PEO particles which attributes to the PEO electrolyte continuous decomposition. In comparison, the LiF signal detected in the inner CEI of NCM-PEO particles is also weaker than that of NCM-PEOC$_{15}$ particles. Evidently, the organic-rich CEI with less component of inorganic components is unstable for long-time operation. In addition, the stronger signal of TM-C in the C 1s of inner CEI of NCM-PEO particles further illustrates the severe transition metal dissolution. The depth profiles in Figure 4n,o and 3D reconstruction images in Figure S25 (Supporting Information) obtained by TOF-SIMS visually show the distribution of organic and inorganic components in CEI after cycling with different SPEs. A dominated content of LiF (LiF$_2^-$) distributes in the CEI of NCM-PEOC$_{15}$ particles, while a few counts of LiF are found on the outer CEI of NCM-PEO particles. Although the polymer decomposition is unavoidable, the organic species (C$_2$HO$^-$) obviously exist in the CEI of NCM-PEO particles, while only

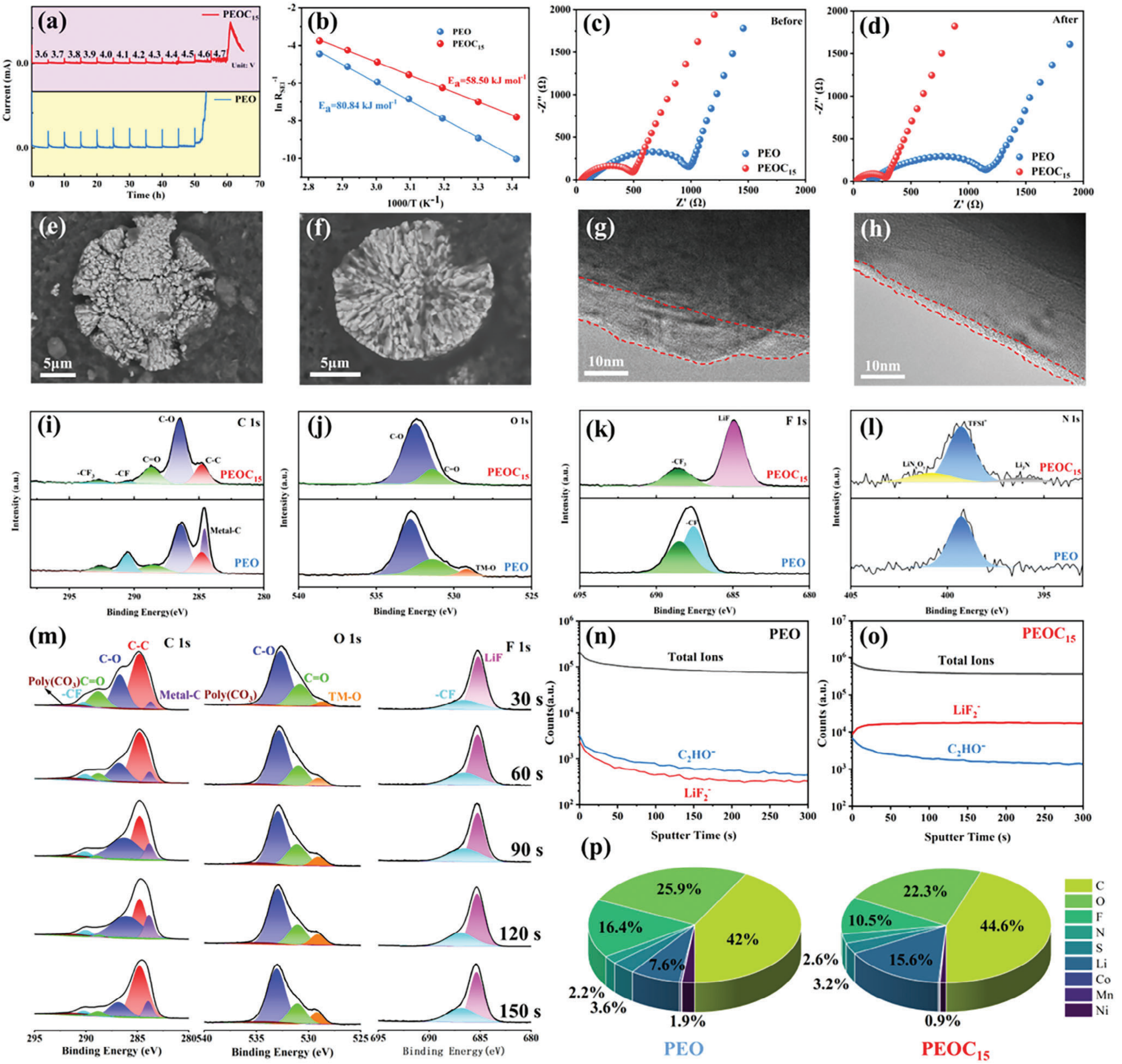

Figure 4. The investigation of stable CEI for suppression the continuous electrolyte decomposition and transition-metal crosstalk. a) Electrochemical floating analysis of NCM811||PEO||Li and NCM811||$PEOC_{15}$||Li batteries at 60 °C. b) Linearly fitted graph of the relationship between ln ($R_{SEI}{}^{-1}$) and T^{-1}. Nyquist plots of the NCM811||PEO||Li and NCM811||$PEOC_{15}$||Li batteries c) before and d) after 100 cycles. SEM images of cycled NCM811 particles with e) PEO and f) $PEOC_{15}$ electrolytes. TEM images of cycled NCM811 particles with g) PEO and h) $PEOC_{15}$ electrolytes. High-resolution XPS spectra of NCM811 particles after cycling with the PEO and $PEOC_{15}$: i) C 1s, j) O 1s, k) F 1s, and l) N 1s. m) High-resolution XPS spectra of C 1s, O 1s, and F 1s of cycled NCM811 particles with $PEOC_{15}$ electrolyte at various sputtering times. TOF-SIMS depth profiles of the cycled NCM811 cathode surface with n) PEO and o) $PEOC_{15}$ electrolytes. p) Elemental contents of cycled Li surface in NCM811||PEO||Li and NCM811||$PEOC_{15}$||Li batteries.

concentrated distribution on the outer CEI of NCM-$PEOC_{15}$ particles. Also, we calculated the anode element contents of the cycled NCM811||Li batteries with PEO and $PEOC_{15}$ electrolytes in accordance with XPS spectra. The lower Ni content of lithium anode cycled with $PEOC_{15}$ electrolyte illustrates the transition-metal crosstalk is inhibited (Figure 4p), which may because the dissolutive TMs are captured and stabilized by 15-crown-5.[48]

2.4. Performance Evaluation of All-Solid-State Batteries

Since the 15-crown-5 is beneficial for enhancing lithium-ion transport and regulating interfacial chemistry, the $PEOC_{15}$ electrolyte was applied in the full all-solid-state batteries to evaluate the electrochemical performances. **Figure 5a–c** presents the long-term cycling and rate performances of the assembled NCM811||$PEOC_{15}$||Li and NCM811||PEO||Li batteries.

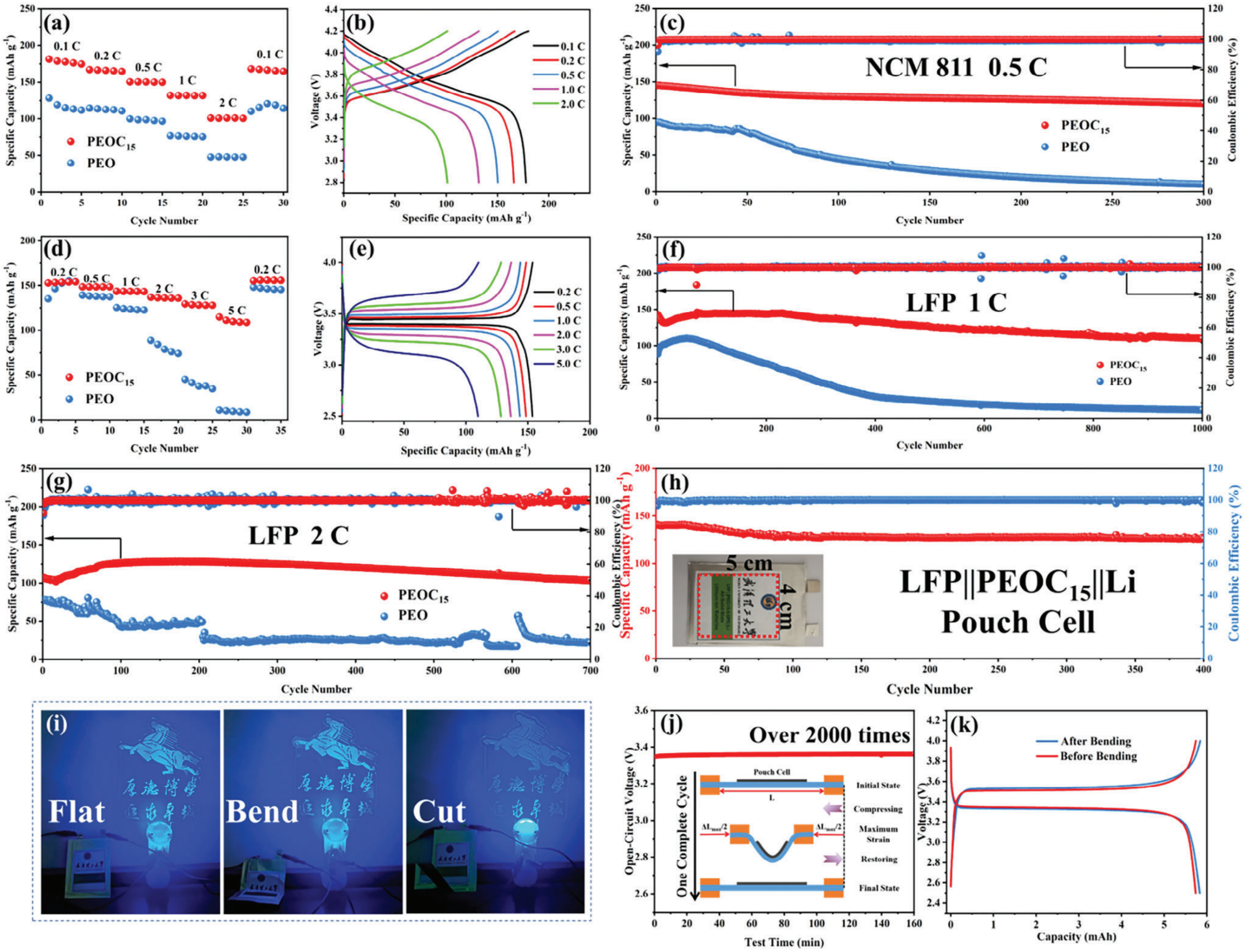

Figure 5. High-rate, stable, and flexible of all-solid-state batteries. a) Rate performance of NCM811||Li batteries with PEO and PEOC$_{15}$ electrolytes at different rates. b) Voltage–capacity profiles of NCM811||PEOC$_{15}$||Li all-solid-state full cells at different rates. c) Cycling performance of NCM811||Li batteries with PEO and PEOC$_{15}$ electrolytes at 0.5 C. d) Rate performance of LiFePO$_4$||Li batteries with PEO and PEOC$_{15}$ electrolytes at different rates. e) Voltage–capacity profiles of LiFePO$_4$||PEOC$_{15}$||Li all-solid-state full cells at different rates. Cycling performance of LiFePO$_4$||Li batteries with PEO and PEOC$_{15}$ electrolytes at f) 1 C and g) 2 C. h) Cycling performance of assembled 5 cm × 4 cm LiFePO$_4$||PEOC$_{15}$||Li pouch cell. i) The assembled LiFePO$_4$||PEOC$_{15}$||Li pouch cell lights up the LED board at the flat, bend, and cut states. j) The open-circuit voltage of the pouch cell during the cycled bending test. k) Typical charge–discharge profiles of pouch cell before and after bending for 2000 times.

The discharge capacities of the battery employed PEOC$_{15}$ electrolyte at 0.1 C, 0.2 C, 0.5 C, 1 C, and 2 C are 177.7, 165.9, 150.2, 131.8, and 101.1 mAh g^{-1}, respectively, which outclasses that of the battery employed PEO electrolyte. After 300 cycles at 0.5 C, the NCM811||PEOC$_{15}$||Li battery maintains a capacity retention of 83.17%. However, the NCM811||PEO||Li presents an initial specific capacity of 94.9 mAh g^{-1}, and falls off rapidly. The differences indicate the high voltage stability of the PEOC$_{15}$ electrolyte. In addition, the NCM811||PEOC$_{15}$||Li battery also can be stably operated in 4.3 V (Figure S26, Supporting Information). When PEOC$_{15}$ electrolyte applying in LiFePO$_4$||Li batteries, the discharge capacities battery at 0.2 C, 0.5 C, 1 C, 2 C, 3 C, and 5 C are 153.6, 148.4, 143.5, 136.1, 128.2, and 109.7 mAh g^{-1} respectively, and also delivered superior capacity reversibility when current density set back to 0.2 C (155.8 mAh g^{-1}). Obviously, the maximum discharge rate of LiFePO$_4$||Li full batteries with PEOC$_{15}$ is 5 C. For comparison, the discharge capacity of LiFePO$_4$||PEO||Li battery begins to sharping drop down when the rate is just higher at 2 C (Figure 5d,e). At a rate of 1 C, the assembled LiFePO$_4$||PEOC$_{15}$||Li battery presents a maximum specific capacity of 144.4 mAh g^{-1} and after an ultra-long cycle life of 1000 cycles still delivers 109.8 mAh g^{-1} (Figure 5f). The battery employed PEOC$_{15}$ as an electrolyte possesses a maximum specific capacity of 128.0 mAh g^{-1} at 2 C and satisfactory capacity retention of 97.18% after 700 cycles (Figure 5g). On the contrary, there is a decline of specific capacity apparently when LiFePO$_4$||PEO||Li battery works at 1 C and hardly operates at a rate of 2 C. Since the high-rate and long-life characteristic of coin cells using PEOC$_{15}$ electrolytes, pouch cells were further assembled to demonstrate the commercial potential. The digital image shown in Figure S27 (Supporting Information) indicates the pouch cell initially exhibited an open-circuit voltage of 3.42 V.

We first employed such a 5 cm × 4 cm pouch cell to investigate the cycling performance. The initial specific capacity of the pouch cell is achieved to 140.8 mAh g^{-1} at 0.1 C, and after 400 cycles, the capacity retention maintains at 89.42% (Figure 5h). The light-emitting diode (LED) board was also lightened by using the pouch cell. When encountering the folding and cutting of the pouch cell, the LED board was still light, and the brightness seemed to hardly weaken, which reflects the safety of $PEOC_{15}$ electrolytes utilization (Figure 5i). Finally, the flexibility of the pouch cell was tested. As can be seen in Figure 5j, the open-circuit voltage hardly changed when the pouch cell was folding by circles. The capacity change of the pouch cell after folding for 2000 times is not clearly observed in Figure 5k.

3. Conclusion

In summary, the 15-crown-5 was introduced to polymer electrolytes for solving the electrode/electrolyte interface stability problem because of the electrolyte decomposition and lithium dendrites. The 15-crown-5 possesses the molecule crowding effect due to the superior compatibility with polymer and electrostatic repulsion for anion, leading the abundant anions to be limited in the Li^+ coordinated sheath to form anion-rich coordinated structure for enhancing the lithium-ion transport and regulating the interfacial chemistry. The 15-crown-5 promotes the dissociation of Li salts, weakens the Li–EO coordination, and vastly destroys the crystalline region of the PEO matrix, resulting in enhanced Li^+ concentration, fast Li^+ transport, and broadened Li^+ transport pathways in the electrolyte. The LiF-rich SEI layer with a fast Li^+ diffusion rate is formed by the decomposition of confined anions, resulting in uniform lithium deposition. The inorganic compound contents in SEI boost Young's modulus to prevent the lithium dendrites' growth and penetration of the interface. Also, the thin and tough CEI presents a LiF-rich inner, which prevents polymer electrolyte continuous degradation and transition-metal crosstalk. As a result, the lithium symmetric cell possesses ultra-stability by maintaining over 4360 h without short-circuit. The assembled $LiFePO_4||PEOC_{15}|||Li$ coin batteries present the characteristics of high rate and long life. The $LiNi_{0.8}Co_{0.1}Mn_{0.1}O_2||PEOC_{15}||Li$ full batteries also show satisfactory capacity retention cycling at high voltage. The pouch cells deliver favorable flexibility and safety and can operate at both normal and extreme conditions. Also, this work provides a practical application for boosting the interfacial stability of all-solid-state electrolytes by modulating the ion environment and then regulating the interfacial chemistry at the molecular level.

Supporting Information

Supporting Information is available from the Wiley Online Library or from the author.

Acknowledgements

This work was financially supported by the National Key Research and Development Program of China (2020YFA0715000), the National Natural Science Foundation of China (52272234), the Key Research and Development Program of Hubei Province (2021BAA070), Independent Innovation Projects of the Hubei Longzhong Laboratory (2022ZZ-20), the Sanya Science and Education Innovation Park of Wuhan University of Technology (2021KF0011).

Conflict of Interest

The authors declare no conflict of interest.

Data Availability Statement

The data that support the findings of this study are available from the corresponding author upon reasonable request.

Keywords

15-crown-5, all-solid-state lithium batteries, interface stability, interfacial chemistry, molecule crowding strategy

Received: March 15, 2024
Revised: May 21, 2024
Published online: June 11, 2024

[1] X. He, D. Bresser, S. Passerini, F. Baakes, U. Krewer, J. Lopez, C. T. Mallia, Y. Shao-Horn, I. Cekic-Laskovic, S. Wiemers-Meyer, F. A. Soto, V. Ponce, J. M. Seminario, P. B. Balbuena, H. Jia, W. Xu, Y. Xu, C. Wang, B. Horstmann, R. Amine, C.-C. Su, J. Shi, K. Amine, M. Winter, A. Latz, R. Kostecki, *Nat. Rev. Mater.* **2021**, *6*, 1036.

[2] M. Jiang, D. L. Danilov, R. Eichel, P. H. L. Notten, *Adv. Energy Mater.* **2021**, *11*, 2103005.

[3] a) J. Yan, H. Huang, J. Tong, W. Li, X. Liu, H. Zhang, H. Huang, W. Zhou, *Interdiscip. Mater.* **2022**, *1*, 330; b) Z. Cui, A. Manthiram, *Angew. Chem., Int. Ed.* **2023**, *62*, 202307243.

[4] a) W. Xia, Y. Zhao, F. Zhao, K. Adair, R. Zhao, S. Li, R. Zou, Y. Zhao, X. Sun, *Chem. Rev.* **2022**, *122*, 3763; b) F. Han, A. S. Westover, J. Yue, X. Fan, F. Wang, M. Chi, D. N. Leonard, N. J. Dudney, H. Wang, C. Wang, *Nat. Energy* **2019**, *4*, 187; c) Y. Guo, S. Wu, Y.-B. He, F. Kang, L. Chen, H. Li, Q.-H. Yang, *eScience* **2022**, *2*, 138.

[5] a) Q. Zhao, S. Stalin, C.-Z. Zhao, L. A. Archer, *Nat. Rev. Mater.* **2020**, *5*, 229; b) A. Manthiram, X. Yu, S. Wang, *Nat. Rev. Mater.* **2017**, *2*, 16103.

[6] a) D. M. Reinoso, M. A. Frechero, *Energy Storage Mater.* **2022**, *52*, 430; b) X. Lu, Y. Wang, X. Xu, B. Yan, T. Wu, L. Lu, *Adv. Energy Mater.* **2023**, *13*, 2301746.

[7] S. Zhang, T. Liang, D. Wang, Y. Xu, Y. Cui, J. Li, X. Wang, X. Xia, C. Gu, J. Tu, *Adv. Sci.* **2021**, *8*, 2003241.

[8] D. H. S. Tan, A. Banerjee, Z. Chen, Y. S. Meng, *Nat. Nanotechnol.* **2020**, *15*, 170.

[9] Z. Li, H. Zhang, X. Sun, Y. Yang, *ACS Energy Lett.* **2020**, *5*, 3244.

[10] a) P. Ding, Z. Lin, X. Guo, L. Wu, Y. Wang, H. Guo, L. Li, H. Yu, *Mater. Today* **2021**, *51*, 449; b) L. Xu, S. Tang, Y. Cheng, K. Wang, J. Liang, C. Liu, Y.-C. Cao, F. Wei, L. Mai, *Joule* **2018**, *2*, 1991. c) X. Miao, S. Guan, C. Ma, L. Li, C. Nan, *Adv. Mater.* **2023**, *35*, 2206402.

[11] Q. Ye, H. Liang, S. Wang, C. Cui, C. Zeng, T. Zhai, H. Li, *J. Energy Chem.* **2022**, *70*, 356.

[12] D. Cao, X. Sun, Q. Li, A. Natan, P. Xiang, H. Zhu, *Matter.* **2020**, *3*, 57.

[13] H. Liu, X.-B. Cheng, J.-Q. Huang, H. Yuan, Y. Lu, C. Yan, G.-L. Zhu, R. Xu, C.-Z. Zhao, L.-P. Hou, C. He, S. Kaskel, Q. Zhang, *ACS Energy Lett.* **2020**, *5*, 833.

[14] H. Xu, H. Zhang, J. Ma, G. Xu, T. Dong, J. Chen, G. Cui, *ACS Energy Lett.* **2019**, *4*, 2871.

[15] J. Pan, P. Zhao, N. Wang, F. Huang, S. Dou, *Energy Environ. Sci.* **2022**, *15*, 2753.

[16] R. Sim, L. Su, A. Dolocan, A. Manthiram, *Adv. Mater.* **2023**, *15*, 2311573.

[17] a) X. Wang, Y. Song, X. Jiang, Q. Liu, J. Dong, J. Wang, X. Zhou, B. Li, G. Yin, Z. Jiang, J. Wang, *Adv. Funct. Mater.* **2022**, *32*, 2113068; b) S. Han, B. Wu, H. Wang, P. Wen, L. Zhang, X. Lin, M. Chen, *Angew. Chem., Int. Ed.* **2023**, *62*, 202308724.

[18] a) M. Jia, P. Wen, Z. Wang, Y. Zhao, Y. Liu, J. Lin, M. Chen, X. Lin, *Adv. Funct. Mater.* **2021**, *31*, 2101736; b) S. Zhang, F. Sun, X. Du, X. Zhang, L. Huang, J. Ma, S. Dong, A. Hilger, I. Manke, L. Li, B. Xie, J. Li, Z. Hu, A. C. Komarek, H.-J. Lin, C.-Y. Kuo, C.-T. Chen, P. Han, G. Xu, Z. Cui, G. Cui, *Energy Environ. Sci.* **2023**, *16*, 2591; c) X. Guo, Z. Ju, X. Qian, Y. Liu, X. Xu, G. Yu, *Angew. Chem., Int. Ed.* **2023**, *62*, 202217538.

[19] W. Zhou, Z. Wang, Y. Pu, Y. Li, S. Xin, X. Li, J. Chen, J. B. Goodenough, *Adv. Mater.* **2019**, *31*, 1805574.

[20] F. Liu, Y. Cheng, X. Zuo, R. Chen, J. Zhang, L. Mai, L. Xu, *Chem. Eng. J.* **2022**, *441*, 136077.

[21] a) H. Xu, C. Sun, S. Zhang, H. Zhang, Z. Liu, Y. Tang, G. Cui, *ChemSusChem* **2023**, *16*, 202202334; b) H. Zhang, L. Huang, H. Xu, X. Zhang, Z. Chen, C. Gao, C. Lu, Z. Liu, M. Jiang, G. Cui, *eScience* **2022**, *2*, 201; c) G. Xiao, H. Xu, C. Bai, M. Liu, Y. He, *Interdiscip. Mater.* **2023**, *2*, 609.

[22] X. Yang, M. Jiang, X. Gao, D. Bao, Q. Sun, N. Holmes, H. Duan, S. Mukherjee, K. Adair, C. Zhao, J. Liang, W. Li, J. Li, Y. Liu, H. Huang, L. Zhang, S. Lu, Q. Lu, R. Li, C. V. Singh, X. Sun, *Energy Environ. Sci.* **2020**, *13*, 1318.

[23] F. Zhang, J. Lai, Z. Hu, A. Zhou, H. Wang, X. Hu, L. Hou, B. Li, W. Sun, N. Chen, L. Li, F. Wu, R. Chen, *Angew. Chem., Int. Ed.* **2023**, *62*, 202301772.

[24] D. M. Halat, R. L. Snyder, S. Sundararaman, Y. Choo, K. W. Gao, Z. J. Hoffman, B. A. Abel, L. S. Grundy, M. D. Galluzzo, M. P. Gordon, H. Celik, J. J. Urban, D. Prendergast, G. W. Coates, N. P. Balsara, J. A. Reimer, *Chem. Mater.* **2021**, *33*, 4915.

[25] J. Hoffknecht, A. Wettstein, J. Atik, C. Krause, J. Thienenkamp, G. Brunklaus, M. Winter, D. Diddens, A. Heuer, E. Paillard, *Adv. Energy Mater.* **2023**, *13*, 2202789.

[26] Z. Piao, R. Gao, Y. Liu, G. Zhou, H. Cheng, *Adv. Mater.* **2023**, *35*, 2206009.

[27] H. Wang, X. Li, Q. Zeng, Z. Li, Y. Liu, J. Guan, Y. Jiang, L. Chen, Y. Cao, R. Li, A. Wang, Z. Wang, L. Zhang, *Energy Storage Mater.* **2024**, *66*, 103188.

[28] S. Liu, X. Shen, L. Wei, R. Wang, B. Ding, J. Yu, J. Yan, *Energy Storage Mater.* **2023**, *59*, 102773.

[29] D. Ruan, L. Tan, S. Chen, J. Fan, Q. Nian, L. Chen, Z. Wang, X. Ren, *JACS Au* **2023**, *3*, 953.

[30] O. Sheng, C. Jin, J. Luo, H. Yuan, H. Huang, Y. Gan, J. Zhang, Y. Xia, C. Liang, W. Zhang, X. Tao, *Nano Lett.* **2018**, *18*, 3104.

[31] M. Ma, F. Shao, P. Wen, K. Chen, J. Li, Y. Zhou, Y. Liu, M. Jia, M. Chen, X. Lin, *ACS Energy Lett.* **2021**, *6*, 4255.

[32] S. Sarkar, V. Thangadurai, *ACS Energy Lett.* **2022**, *7*, 1492.

[33] a) S. Liu, Y. Zhao, X. Li, J. Yu, J. Yan, B. Ding, *Adv. Mater.* **2021**, *33*, 2008084; b) W. Li, J. Gao, H. Tian, X. Li, S. He, J. Li, W. Wang, L. Li, H. Li, J. Qiu, W. Zhou, *Angew. Chem., Int. Ed.* **2022**, *61*, 202114805.

[34] P. Zhai, N. Ahmad, S. Qu, L. Feng, W. Yang, *Adv. Funct. Mater.* **2024**, 2316561.

[35] a) X. Liang, Q. Pang, I. R. Kochetkov, M. S. Sempere, H. Huang, X. Sun, L. F. Nazar, *Nat. Energy* **2017**, *2*, 17119; b) Y. Lin, Z. Wen, C. Yang, P. Zhang, J. Zhao, *Electrochem. Commun.* **2019**, *108*, 106565.

[36] M. Zhou, M. Li, Y. Liao, L. Li, R. Xiong, G. Shen, T. Lu, S. Cui, G. Feng, J.-Y. Xie, H. Zhou, Y. Zhang, *ACS Energy Lett.* **2023**, *8*, 4702.

[37] J. Li, Y. Ji, H. Song, S. Chen, S. Ding, B. Zhang, L. Yang, Y. Song, F. Pan, *Nano-Micro Lett.* **2022**, *14*, 191.

[38] Q. Zhou, J. Ma, S. Dong, X. Li, G. Cui, *Adv. Mater.* **2019**, *31*, 1902029.

[39] N. Yao, S. Sun, X. Chen, X. Zhang, X. Shen, Z. Fu, R. Zhang, Q. Zhang, *Angew. Chem., Int. Ed.* **2022**, *61*, 202210859.

[40] a) Z. Li, R. Yu, S. Weng, Q. Zhang, X. Wang, X. Guo, *Nat. Commun.* **2023**, *14*, 482; b) Z. Jiang, H.-J. Guo, Z. Zeng, Z. Han, W. Hu, R. Wen, J. Xie, *ACS Nano* **2020**, *14*, 13784; c) H. Xu, Y. Li, A. Zhou, N. Wu, S. Xin, Z. Li, J. B. Goodenough, *Nano Lett.* **2018**, *18*, 7414; d) J. Zhang, S. Li, X. Wang, S. Mao, J. Guo, Z. Shen, J. Mao, Q. Wu, K. Shen, H. Cheng, Y. Tan, Y. Lu, *Adv. Energy Mater.* **2024**, *14*, 2302587.

[41] Q. Zhang, J. Pan, P. Lu, Z. Liu, M. W. Verbrugge, B. W. Sheldon, Y.-T. Cheng, Y. Qi, X. Xiao, *Nano Lett.* **2011**, *16*, 2016.

[42] S. Liu, X. Ji, N. Piao, J. Chen, N. Eidson, J. Xu, P. Wang, L. Chen, J. Zhang, T. Deng, S. Hou, T. Jin, H. Wan, J. Li, J. Tu, C. Wang, *Angew. Chem., Int. Ed.* **2021**, *60*, 3661.

[43] Y. Liu, X. Xu, O. O. Kapitanova, P. V. Evdokimov, Z. Song, A. Matic, S. Xiong, *Adv. Energy Mater.* **2022**, *12*, 2103589.

[44] a) X. Chen, Y. Yao, C. Yan, R. Zhang, X. Cheng, Q. Zhang, *Angew. Chem., Int. Ed.* **2020**, *132*, 7817; b) J. Sun, J. Peng, T. Ring, L. Whittaker-Brooks, J. Zhu, D. Fraggedakis, J. Niu, T. Gao, F. Wang, *Energy Environ. Sci.* **2022**, *15*, 5284.

[45] L. Du, B. Zhang, C. Yang, L. Cui, L. Mai, L. Xu, *Energy Storage Mater.* **2023**, *61*, 102914.

[46] C. Yang, M. Zheng, R. Qu, H. Zhang, L. Yin, W. Hu, J. Han, J. Lu, Y. You, *Adv. Mater.* **2024**, *36*, 2307220.

[47] J. Yang, X. Liu, Y. Wang, X. Zhou, L. Weng, Y. Liu, Y. Ren, C. Zhao, M. Dahbi, J. Alami, D. A. Ei-Hady, G. Xu, K. Amine, M. Shao, *Adv. Energy Mater.* **2021**, *11*, 2101956.

[48] a) X. Luo, L. Xing, J. Vatamanu, J. Chen, J. Chen, M. Liu, C. Wang, K. Xu, W. Li, *J. Energy Chem.* **2022**, *65*, 1; b) C. Zhao, Y. Lu, K. Yan, Y. Guan, S. Jiang, J. Wang, S. Guo, M. Cao, N. Li, Y. Su, F. Wu, L. Chen, *Adv. Energy Mater.* **2024**, 2304532.